Ultrasonics 94 (2019) 438–453

Contents lists available at ScienceDirect

Ultrasonics

journal homepage: www.elsevier.com/locate/ultras

Initialization of active contours for segmentation of breast cancer via fusion of ultrasound, Doppler, and elasticity images

Chadaporn Keatmanee [a,c], Utairat Chaumrattanakul [b], Kazunori Kotani [c], Stanislav S. Makhanov [a,*]

[a] Sirindhorn International Institute of Technology, Thammasat University, Pathum Thani, Thailand
[b] Department of Radiology, Thammasat University, Pathum Thani, Thailand
[c] Japan Advanced Institute of Science and Technology, Ishikawa, Japan

ARTICLE INFO

Article history:
Received 3 August 2017
Received in revised form 15 December 2017
Accepted 19 December 2017
Available online 24 December 2017

Keywords:
Segmentation
Breast cancer
Active contours
Initialization
Ultrasound
Elastography
Doppler image

ABSTRACT

Active contours (snakes) are an efficient method for segmentation of ultrasound (US) images of breast cancer. However, the method produces inaccurate results if the seeds are initialized improperly (far from the true boundaries and close to the false boundaries). Therefore, we propose a novel initialization method based on the fusion of a conventional US image with elasticity and Doppler images. The proposed fusion method (FM) has been tested against four state-of-the-art initialization methods on 90 ultrasound images from a database collected by the Thammasat University Hospital of Thailand. The ground truth was hand-drawn by three leading radiologists of the hospital. The reference methods are: center of divergence (CoD), force field segmentation (FFS), Poisson Inverse Gradient Vector Flow (PIG), and quasi-automated initialization (QAI).

A variety of numerical tests proves the advantages of the FM. For the raw US images, the percentage of correctly initialized contours is: FM-94.2%, CoD-0%, FFS-0%, PIG-26.7%, QAI-42.2%. The percentage of correctly segmented tumors is FM-84.4%, CoD-0%, FFS-0%, PIG-16.67%, QAI-22.44%. For reduced field of view US images, the percentage of correctly initialized contours is: FM-94.2%, CoD-0%, FFS-0%, PIG-65.6%, QAI-67.8%. The correctly segmented tumors are FM-88.9%, CoD-0%, FFS-0%, PIG-48.9%, QAI-44.5%. The accuracy, in terms of the average Hausdorff distance, is respectively 2.29 pixels, 33.81, 34.71, 7.7, and 8.4, whereas in terms of the Jaccard index, it is 0.9, 0.18, 0.19, 0.63, and 0.48.

1. Introduction

An annual check for breast cancer includes a mammogram, and ultrasound examination of the breast. The mammogram is considered a primary tool for women who display no symptoms of the disease [1]. However, if the findings are uncertain, a woman may be called for further tests, which include extra mammographic views and breast ultrasound. Therefore, in practice, ultrasound is an additional tool, which is important in cases of dense breasts (young women).

Along with the conventional US imagery, modern US machines produce Elastography and Doppler images, which in many cases improve the quality of the diagnosis [21]. Elastography is used as an adjunct technique to help in discrimination between benign and malignant masses, based on their stiffness [84]. Power Doppler is another non-invasive US modality which supplements conventional US. Doppler images visualize the appearance and morphology of blood vessels associated with a mass. The analysis uses the fact that a benign mass has little or no vascular flow, whereas a malignancy increases the blood flow in the vicinity of the tumor [15].

Since the Elastography and Doppler images are usually available in cases when cancer is suspected, we propose to use them, along with a conventional US image to improve the quality of automatic segmentation of breast tumors. In particular, we focus on the fusion of the US, elasticity, and Doppler images in the framework of active contours (snakes) [43]. Active contours are one of the most popular segmentation techniques applied to many image processing problems, originating from different applications. The most successful modifications of the active contours are the gradient vector flow (GVF) snakes [90], generalized gradient vector flow snakes (GGVF) [89], multidirectional GGVF snakes [76], Vector Field Convolution snakes (VFC) [48], and the recent Adaptive Diffusion Flow snakes (ADF) [87].

However, the accuracy and computational time of the above mentioned models depend on the initial location (seed snakes). Unfortunately, if the seeds are far from the boundary of the object,

* Corresponding author.
E-mail address: makhanov@siit.tu.ac.th (S.S. Makhanov).

https://doi.org/10.1016/j.ultras.2017.12.008
0041-624X/

the snake can attach itself to false boundaries. Modern US/sharewave machines generate three types of the images mentioned above. Each of them helps radiologists to localize and classify a tumor i.e. the tumors characterized by the low intensity of the gray level in the US image, high stiffness in the elasticity image, and by an increased vascularity in the Doppler images. Therefore, we introduce a novel initialization method based on the fusion of the conventional US, elasticity and Doppler images. The proposed algorithm combines the images by means of a distance transform and a low intensity mask to generate a suitable initial contour and a supplementary balloon force. A video demo of the algorithm is at https://drive.google.com/file/d/13DWNibnMPc_P8nKn6TGfvObQD0ngZko2.

2. Related work

Segmentation of breast abnormalities has received considerable attention in the literature. An extensive review by Noble and Boukerroui [65] mentions that such segmentation can be treated as a general image processing problem and includes a priori information of ultrasound. The segmentation algorithms include numerous modifications of the conventional thresholding, neural networks (see a concise survey in [72]), watershed techniques [35], statistical methods [8,54], active contours (see extended surveys [13,30], and a large list of references compiled in [68]), level set method (see recent surveys in [28,29]), and graph-based segmentation refined by active contours [34]. Excellent results have been obtained by combining a modified watershed model and all tissue classification for segmentation of 3D US images [26].

However, among these segmentation techniques, neural networks and other AI based methods require feature selection and training. Initial seeds are required for the watershed and graph-based methods, as well as for the active contours and the level-set methods. Finally, an unsupervised Fuzzy C-means method (FCM) is a good alternative to techniques requiring prior information, training, and initial contours (see, a concise review in [23]). In particular, Feng et al. [23] develops a new modification of the FCM based on Hausdorff distance and an adaptive selection of the neighbor region of each pixel for distance measurement and centroid updating. However, the classical disadvantages of the FCM are still a long computational time and relatively high sensitivity to the initial guess.

Apart from active contours, the proposed FM is potentially applicable to all of the above mentioned techniques, in particular to the watershed, level set initialization, and even to conventional or adaptive thresholding. We may conjecture that the FCM could also benefit from the FM since basically, the initial contour provides additional information about a possible location of the tumor. However, such combinations are out of the scope of this paper. Our focus is the initial seeds for the active contours.

Let us review some ideas developed specifically for active contours. One of the most popular techniques is analysis of the vector field generated by the GVF-type model [90]. For instance, Li et al. [50] applies FFS to divide the image domain into disjointed regions representing the capture range of the external force field. The snakes can be individually initialized within each of the enclosures and moved to the targeted object boundary within it, avoiding being attracted by other objects. However, the algorithm transforms an image segmentation problem into a vector field segmentation problem, which is difficult to solve if strong noise is present.

The idea to initialize the snakes at the CoD of the GVF-type vector field was first mentioned in [83]. Further, Ge and Tan [88] define the CoD by analyzing relative directions of the vector field in a sliding 2×2 window (a generalization to larger windows is not available). He et al. [95] uses Phase Portrait Analysis (PPA) [74] to detect the critical points of the vector field and a rule that "the initial contours should be set to contain all of the node points in the object area and none of the others". Although PPA has been used in a variety of image processing applications, e.g. [16,51,52,74,80,93], the standard PPA classifier based on "if then" rules often cannot be adapted to the case of snake initializations characterized by irregular nodes corrupted by noise.

The similarity of the GGVF and the Navier-Stokes equations makes it possible to use the analogy of a flow through a porous medium. Consequently, Ray et al. [67] treats the initial snakes as sources of flow, emitting normal unit vectors into the image domain. The authors also noticed critical points of the flow and proposed to merge multi-snakes, initialized around those points for segmentation of the MRI images of lungs.

A competing idea is placing the seed points uniformly or randomly over the entire image, evolving them from each seed point, and analyzing the resulting configuration [70]. However, the required classifier to validate the final configuration must be trained, which makes the model image-dependent.

A partial solution to the problem is the above mentioned QAI method by Tauber et al. [78,79]. The method employs the CoDs combined with a tracing procedure to create a "skeleton" of the object, consisting of centers of strong and weak divergence. The centers of weak divergence are the points where the vectors of the GVF diverge in one (either horizontal or vertical) direction. The centers of strong divergence feature both horizontal and vertical divergences. The initial snake is generated around the skeleton. However, the initialization is not entirely automatic. The algorithm still requires at least one manually generated point inside the object. Moreover, in some cases the skeleton can evolve outside the boundary of the object.

The above mentioned PIG model [49] establishes the relationship between the external force field and the underlying external energy field via the solution of the corresponding Poisson equation. The model has been applied to 2D and 3D cases for a variety of medical images. The isoline of the minimum energy is selected as the initial contour. However, the model may suffer from incomplete isolines, as well as from over segmentation.

An automatic initialization method has been proposed in [32] for PET images of the liver. The candidate contours are generated by Canny edge detection and subsequently classified by a genetic algorithm. The algorithm has been applied to segmentation of face contours in video files [33]. A similar idea was introduced in [81] for detection of the synovial boundaries in US images. However, the initial snakes selected from the edge map are not robust and may not be applicable to multiple objects.

The idea of trial snakes (TS), combined with PPA, was applied to US images of breast cancer in [44]. The PPA makes it possible to detect the centers of convergence and divergence, as well as the attracting and repelling nodes. The algorithm differentiates between the internal and external seeds by running multiple TS from the critical points and checking their intersections with the boundary of the image. The most serious drawback of TS is that they require a considerable amount of computational time.

The initialization algorithms for the US images often rely on gray levels and textures, to place the seed points inside the tumor [19,41,58]. Saliency and feature maps have been proposed in [71]. Fergani et al. [24] introduces a special vector field to hybridize the GVF and the texture. A Chan-Vese type model is proposed in [55]. A few papers related to a specific medical image processing task use the typical position of a human organ in the US images (see, for instance, Akgul et al. [3]). However, these models are image dependent and may not work if strong noise is present.

Therefore, this paper proposes a new fast algorithm for automatic initialization, which combines the conventional grayscale US image with the corresponding elasticity and Doppler images.

The technique makes it possible to locate the initial contour inside the tumor, close enough to the true boundaries to ensure convergence of the active contour. The paper also introduces a modification of the balloon type active contour, based on a combination of the radial force derived from the fusion image and the GVF-type force.

3. Background

3.1. Ultrasonography for breast cancer screening

The World Health Organization reports that breast cancer is common in women. The cases of breast cancers in developing countries are increasing due to the increase in life expectancy, urbanization, and western lifestyles [86]. The mammogram remains the primary screening tool for women who display no symptoms of the disease [1]. However, high-resolution US is considered one of the most appropriate adjunct tools [73,69] due to a number of advantages, such as no exposure to radiation, simplicity, and low cost. Besides, in dense breasts, mammography has limited sensitivity, whereas US is useful to examine dense breast tissue. Note that women with dense parenchyma have an increased risk of breast cancer. Recent studies have shown that the detection of small cancers with high-resolution US has increased by 3–4 cancers per 1000 women without clinical or mammographic abnormalities [59]. Apart from screening, US is used in daily practice, in order to improve lesion detection and characterization. Several large studies have shown a possible role of US for cancer detection and differentiation e.g. [45]. Thus, computer aided diagnosis, including US imaging, is likely to improve survival rates [62,63].

3.1.1. Elastography

Elastography (Fig. 1(b)) is a US imaging modality to classify breast masses based on their stiffness [37,91]. A US machine displays a color elastography image as follows [39]:

Score 1: blue indicates soft and loose structures.
Score 2: a combination of blue and green indicates soft-rigid structures.
Score 3: red and dark red at the center of the mass, and green at the periphery, indicate a hard to soft mass.
Score 4: red and dark red indicates a hard and tight mass.
Score 5: red and dark red covering the mass and the surrounding tissue refer to a hard expanding mass. Scores 1, 2, and 3 represent benign features, whereas masses scoring 4 and 5 are likely to be malignant [4,5,91].

Note that some machines display the stiffness in the reverse palette, i.e. blue indicates the hardest tissue, whereas red indicates the soft tissue.

3.1.2. Power Doppler imaging

Power Doppler (Fig. 1(c)) is another non-invasive supplement to the conventional US. The sound waves bounce off solid objects, including blood cells. The movement of the blood cells causes a change in the pitch of the reflected sound waves as a result of the Doppler effect. Typically, a benign mass has little or no appearance of vascular flow, whereas a malignant mass is often characterized by an increased blood flow. The advantages of Power Doppler are high sensitivity, low angle dependency, and no aliasing [64,92]. Therefore, it is also used as an adjunct image modality for breast cancer diagnosis [64,38]. When the cells move towards the transducer, the frequency of returning ultrasound waves is greater than that of the emitted waves, and the blood flow is depicted in red. When the cells move away the flow is depicted in blue. The intensity of the color is proportional to the flow velocity [66]. However, in this paper, we do not analyze the Doppler palette. We only register the presence or absence of the Doppler spots.

3.1.3. Combination of the imaging modalities in clinical practice

The efficiency of combined US, Doppler, and elasticity imaging in diagnosing breast malignancy is still controversial. For instance, Davoudi et al. [18] reports that “using the Doppler image alone has little value in differentiating between malignant and benign breast lesions”. The research conducted by [25] concludes that Doppler imaging does not contribute to categorization of solid breast masses. However, there is growing evidence that analysis of a combination of images improves the characterization of breast lesions. Thomas et al. [79] reports that sensitivity/specificity was 96%/68% for US, 100%/40% for US and mammography, and 96%/80% for the combined mode, including Doppler. Cho et al. [15] characterizes the results obtained from 5 readers by the area under the receiver operated characteristic curve A_z as follows: “the A_z of the US mode, elastography, and Doppler US (average, 0.844; range, 0.797–0.876) was greater than that of the US mode alone (average, 0.771; range, 0.738–0.798) for all readers”. Li et al. [53] reports “the specificity of making the decision for biopsy increased from 6.5% to 38.7% when US was combined with color Doppler and elasticity without a statistically significant change in sensitivity”. Elkharbotly and Farouk [22] shows that a combined use of US, elasticity, and color Doppler achieved an NPV of 95% “thus allowing sparing of unnecessary invasive diagnostic procedures”. In summary, there is enough evidence that a combination of the conventional US, elastography, and Doppler images improves the accuracy of diagnosis. Therefore, the above imaging modalities will be increasingly used in clinical conditions to allow for computerized segmentation and classification of tumors.

3.2. Combination of the imaging modalities for classification

Combinations of the different US modalities have been used in several classification algorithms. For instance, the conventional

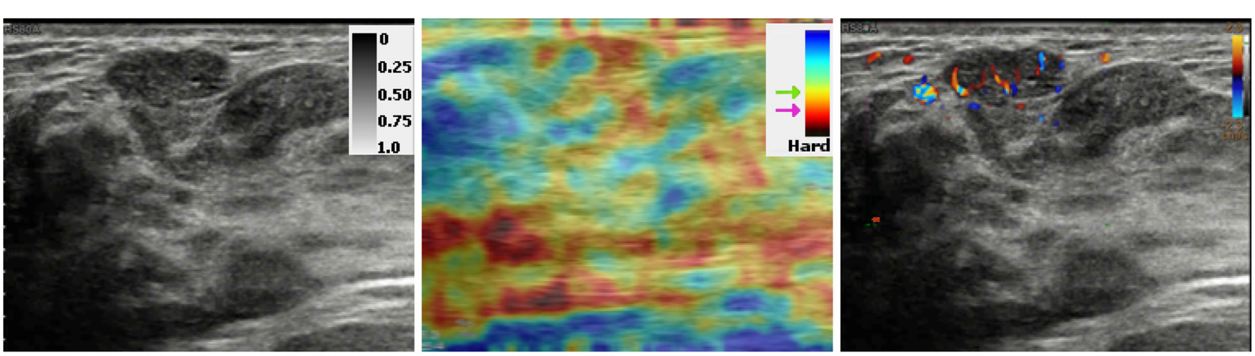

(a) (b) (c)

Fig. 1. Malignant mass. (a) Conventional US, U_{raw}, (b) elastography, E_{raw} (c) Doppler image, D_{raw}.

US and Elastography are used by [7,96], whereas a combination of US and Doppler images is used by [36,31,12,47]. However, the idea of using the three modalities for initialization, and evolving the active contours, seems to be overlooked.

3.3. Active contour model

An active contour (snake) is a parametric curve $v(s) = (x(s), y(s))$ which grows or contracts inside an image to attach itself to the boundary of the desired object. The evolution of the snake is simulated by Euler equations for the energy functional, given by

$$E = \int_0^1 \left[\frac{1}{2}(\alpha \cdot |v_s(s)|^2 + \beta \cdot |v_{ss}(s)|^2) + E_{ext}(v(s))\right] ds, \quad (1)$$

where the subscripts denote partial derivatives, α and β are weighting parameters to control the snake's tension and rigidity, and $E_{ext}(v(s))$ is the external force. The most successful modifications of the active contours are Gradient Vector Flow (GVF) snakes [90], Generalized Gradient Vector Flow (GGVF) snakes [89], multidirectional GGVF snakes [76], and the non-linear diffusion model [85]. Recent GVF-type models are Normal Gradient Vector Flow [40], Infinity Laplacian [27], Harmonic Gradient Vector Flow [82], Convolution Vector Flow [48], Dynamic Directional Gradient Vector Flow [14], Adaptive Diffusion Flow [87], and Multi Feature Gradient Vector Flow [68].

4. Method

This section presents a new initialization method, based on the fusion of the US, elasticity, and Doppler images.

4.1. Preprocessing

The proposed algorithm preprocesses the three types of images introduced above as follows: **US image** (Fig. 1(a)):

$$U_{mask} = \text{Binarize}(\text{Gaussian}(U_{raw})). \quad (2)$$

After Gaussian smoothing, the US image is binarized, creating a low intensity mask (see Fig. 2(b)). Alternatively, one can generate the low intensity mask by (Fig. 2(c)):

$$U_{mask} = \text{RegionGrowing}((\text{Binarize}(U_{raw}))). \quad (3)$$

The mask applies to an image I as follows:

$$\text{Mask}(I_{i,j}) = \begin{cases} I_{i,j}, & \text{if } U_{mask,i,j} = 1, \\ 0, & \text{otherwise.} \end{cases} \quad (4)$$

The **edge map** is generated using Fuzzy C-means clustering [6] (see Fig. 2(a)).

$$U_{edge} = \text{EdgeMap}(U_{raw}). \quad (5)$$

The red channel of the **elasticity image** is binarized (Fig. 3(a)). The resulting output image (Fig. 3(b)) is obtained by applying the low intensity mask (see Figs. 1(b) and 2(b)):

$$E = \text{Mask}(\text{Binarize}(\text{Red}(E_{raw}))). \quad (6)$$

The areas characterized by an increased blood flow are represented by colored spots superimposed on U_{raw}. The **Doppler Image** (Fig. 1(c)) is converted into grayscale and binarized, using an automatic threshold (see Fig. 4(a)). The low intensity mask is then applied to the resulting image (see Fig. 4(b)):

$$D = \text{Mask}(\text{Binarize}(\text{GrayScale}(D_{raw}))). \quad (7)$$

Elimination of outliers is performed by following [10,11] using the Mahalanobis distance [60] and 97.5%-quantile of the Chi-square distribution (Fig. 4(c)).

4.2. Distance transform. Soft intersection

The distance transform is defined with regard to a prescribed set of points S as follows:

$$d_S(P) = \min_S \|P - S\|, \quad (8)$$

where $\|\ \|$ denotes the Euclidean distance and P is an arbitrary point. In image processing, the set S usually is an object (and possibly noise), and P is a point in the binarized image. Consider a normalized $d_S(P)$, so that $\max d_S(P) = 1$. In the forthcoming figures, $d_S(P)$ is represented by a grayscale image, which indicates how far a particular point P is from set S. Clearly, $d_S(S) = 0$. An introductory example is shown in Fig. 5.

Define the fusion image by a soft intersection of d_U, d_E, and d_D:

$$d_F(P) = w_U d_U(P) + w_E d_E(P) + w_D d_D(P), \quad (9)$$

where $d_U(P), d_E(P)$, and $d_D(P)$ are the distance transforms, corresponding to U_{edge}, E, and D, respectively, and w_U, w_E, w_D are the weighting coefficients: $w_U + w_E + w_D = 1$ (Fig. 6(a)-(d)). In practice we use a simple average $w_U = w_E = w_D = \frac{1}{3}$. The contribution of each image to the fusion image is illustrated in Fig. 7. As a variant, d_U, d_E, and d_D can be regarded as the RGB colors, and $d_F(P)$ as a function to convert RGB image to grayscale. Using this analogy, $d_F(P)$ can also be defined similarly to the lightness conversion method [42]:

$$d_F(P) = (\max(d_U(P), d_E(P), d_D(P)) + \min(d_U(P), d_E(P), d_D(P)))/2. \quad (10)$$

The numerical experiments show that the above fusion formulas (9) and (10) produce very close results. Our forthcoming section "Results and discussion" illustrates the proposed FM applied with the soft intersection (9). Fig. 8 demonstrates the advantages of

(a) (b) (c)

Fig. 2. (a) Edge map (U-image), (b) U_{mask} (Gaussian), (d) U_{mask}(Region Growing).

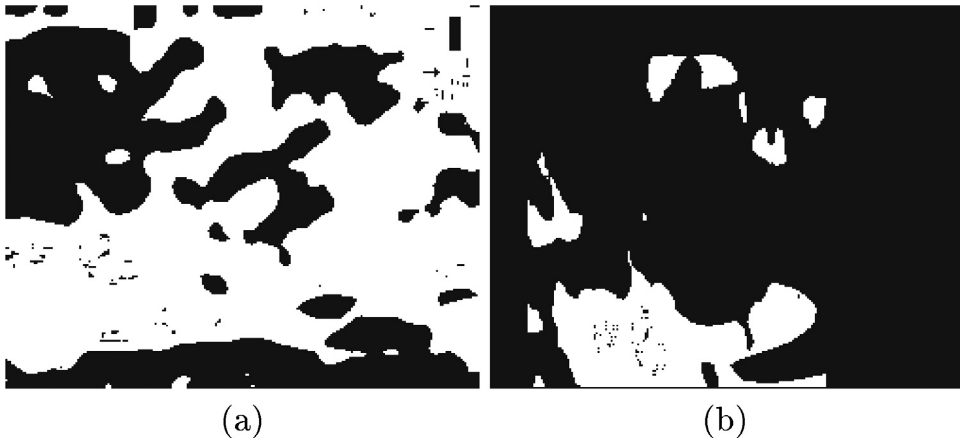

Fig. 3. (a) Binarized elasticity image, (b) E-image.

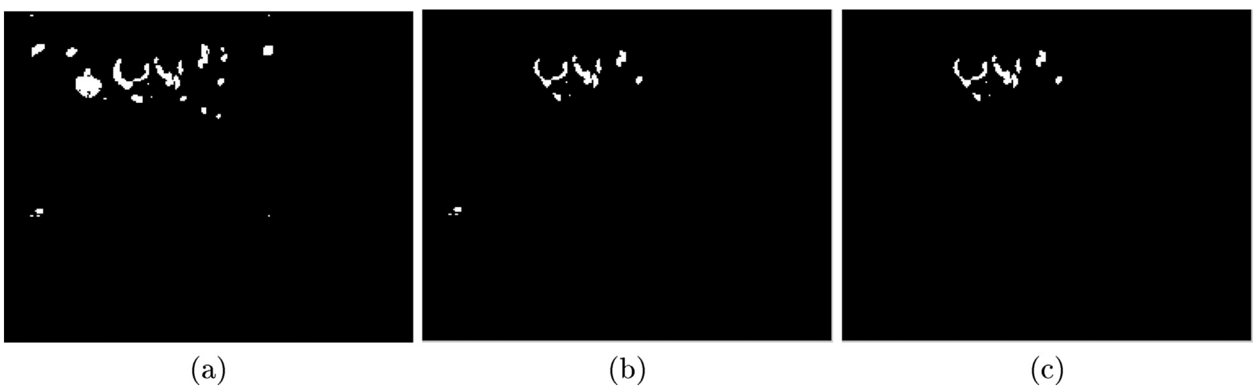

Fig. 4. (a) Binarize(GrayScale(D_{raw})), (b) D = Mask(Binarize(Gaussian(D_{raw}))), (c) D-image, outliers eliminated.

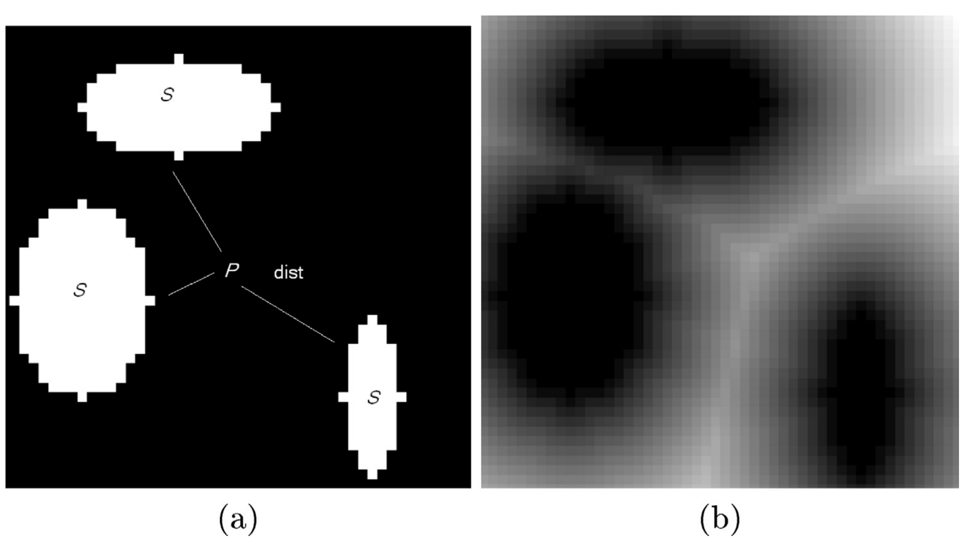

Fig. 5. Example of the distance transform (a) binarized image, (b) distance transform.

the soft intersection for the image in Fig. 1 with reference to the binary intersection. Clearly, the soft intersection in Fig. 8(f) produces an appropriate grayscale image, which can subsequently be used to initialize an active contour, whereas the binary intersections in Fig. 8(d) and (e) are not suitable for initialization.

4.3. Automatic initialization

Consider a sequence of thresholds $\mathbf{T} = T_1, T_2, \ldots T_N$, obtained by an iterative binarization applied to d_F. We apply the Otsu algorithm, employing multiple automatically evaluated thresholds

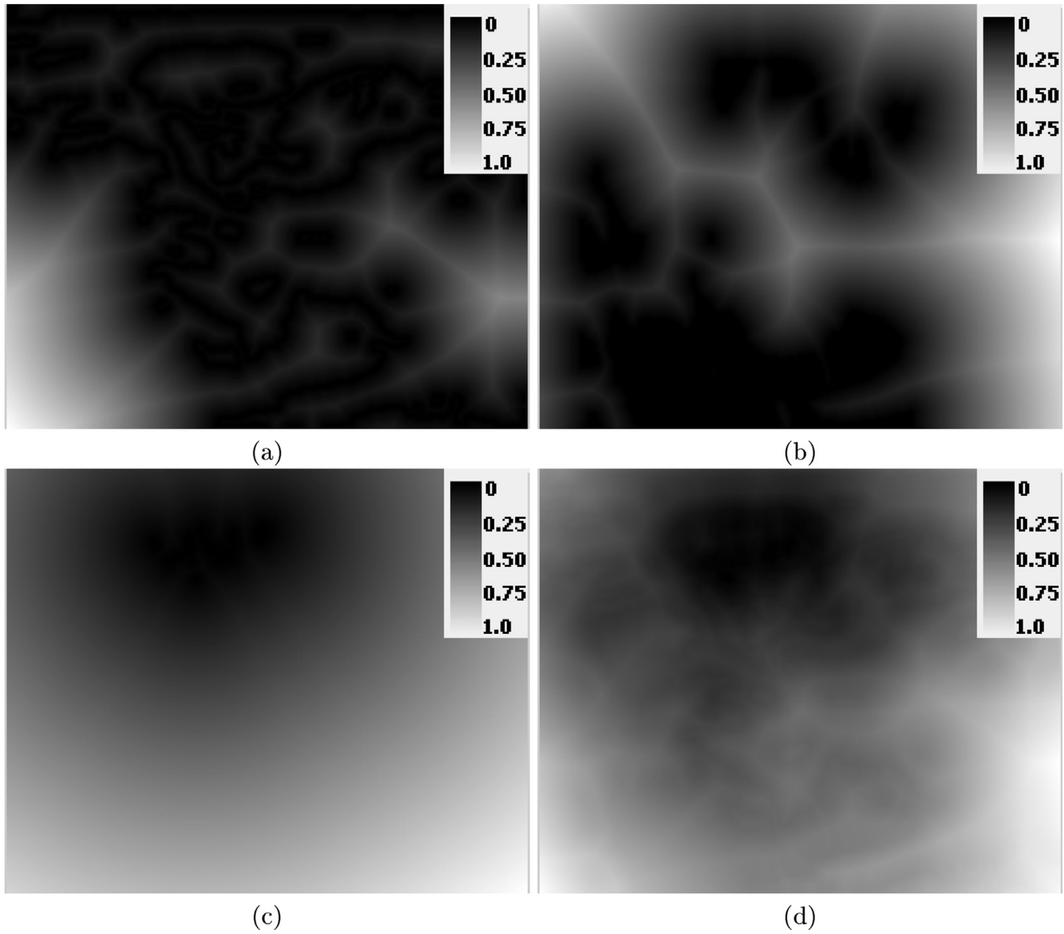

Fig. 6. Distance transforms for the images in Fig. 1: (a) d_U, (b) d_E, (c), d_D, (d) soft intersection d_F.

[94]. Another option is a quantized version of the fusion image, thresholded at N equally spaced levels (Fig. 9):

$$T = \left\{ \frac{\max(d_F)}{N}, \frac{2\max(d_F)}{N}, \ldots, \frac{(N-1)\max d_F}{N} \right\}. \tag{11}$$

Consider a fusion image $d_F(T)$, binarized at the level T. Denote the corresponding edge map by $E_F(T)$ and a set of all continuous contours from $E_F(T)$ by $C_F(T)$. Our basic idea is that the best threshold is the one that generates the closest contour $C_F(T)$ to the convex hull of the Doppler points in the D-image (Fig. 10). Additionally, the contour is verified by a decision tree generated by the CART algorithm [9].

A pseudo-code of the algorithm is given below:

---

input: $U_{raw}, E_{raw}, D_{raw}$
$U, E, D \leftarrow$ preprocess the input images using (5)–(7), respectively
$d_F \leftarrow$ distance transform (9)
$T \leftarrow$ sequence of thresholds (11)
$B_{o,All} \leftarrow$ NULL
$B_D \leftarrow$ convex hull of D
$c_{bd} \leftarrow$ centroid of B_D
for each T_k **in** T
  $d_{F,k} \leftarrow$ threshold d_F
  $E_{F,k} \leftarrow$ edgemap of $d_{F,k}$
  $C_{F,k} \leftarrow$ all continuous contours of $E_{F,k}$ (see Remark 1)
  $B_o \leftarrow$ contour $C_{F,k}$ closest to B_D in terms of the Hausdorff distance $dist_1$
  YesNo $\leftarrow$ evaluate the resulting contour B_o by CART algorithm (decision tree)
  if YesNo $B_{o,All} \leftarrow B_{o,All} + B_o$
if $B_{o,All}$ = NULL
  break
else
  $B_{init} \leftarrow$ contour $B_{All,o}$ closest to B_D, in terms of $dist_1$
$c_o \leftarrow$ centroid of B_{init}
$B_{init} \leftarrow$ contour B_{init} scaled by factor γ, with c_o being the origin
return B_{init}

Remark 1. The procedure to trace the contours is similar to the routine findContours of openCV [46].

We construct the decision tree (DT) using 30 additional US images submitted to the MatLab function **fittree** [61]. The function is designed to implement a conventional CART DT [9,17,56,57] using the Gini index. The DT is based on the following features:

Average gradient of the gray level along B_o relative to the max gradient: $I(T)$.

Ratio of intersection B_o and B_D relative to the B_D : A_{B_o,B_D} = Area $(B_o \cap B_D)$/Area(B_D).

Distance between c_o and c_{bd} : $d_{c_o,c_{bd}}$.

Boolean variable $L = B_D \in B_o$.

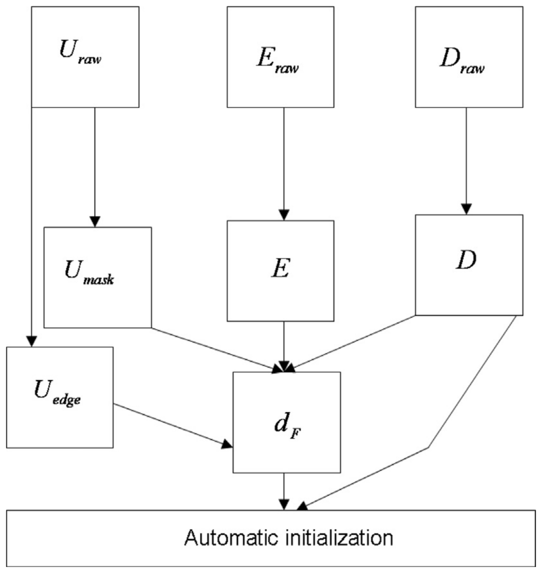

Fig. 7. Generation of the fusion image.

The resulting impurity measures are:
$I_{Gini} = 0.0223, A_{B_O,B_D,Gini} = 0.0199, d_{c_o,c_{bd},Gini} = 0.0239, L_{Gini} = 0.0221.$
The above measures clearly indicate that the resulting DT is a good quality classifier. The corresponding DT and the thresholds are shown in Fig. 11. Note that in order to ensure that B_{init} is inside the tumor, B_o is scaled by factor γ. In principle, γ can be taken sufficiently small so that the snake evolves from the centroid. The FM-balloon force (see the next section) delivers the snake to the boundary, even from a single point. However, in order to improve the computational time, in practice, we use $\gamma = 0.4$.

4.4. Fusion radial force

Recall that the conventional active contour is represented by Eq. (1) [43]. Our proposed external force $E_{ext}(v(s))$ is:

$$E_{ext}(v(s)) = E^1_{ext}(v(s)) + E^2_{ext}(x, y)), \tag{12}$$

where $E^1_{ext}(v(s))$ is the traditional gradient based force, and $E^2_{ext}(x, y))$ is the balloon- type fusion radial force (FRF). The FRF is proportional to the distance between (x, y) and B_o so that $E^2_{ext}(x, y)) = 0$ if $(x, y) \in B_o$ and $E^2_{ext}(x, y)) = E^2_{max}$ if $(x, y) = c_0$, where E^2_{max} is evaluated experimentally (see Fig. 12).

5. Performance measures

In order to compare the fusion method with the conventional algorithms, we introduce the following performance measures.

5.1. Contour based accuracy measures

The Hausdorff distance given by

$$dist_{H_1}(X, Y) = \max\left\{\max_{a\in X}\min_{b\in Y}\|a-b\|, \max_{b\in Y}\min_{a\in X}\|a-b\|\right\} \tag{13}$$

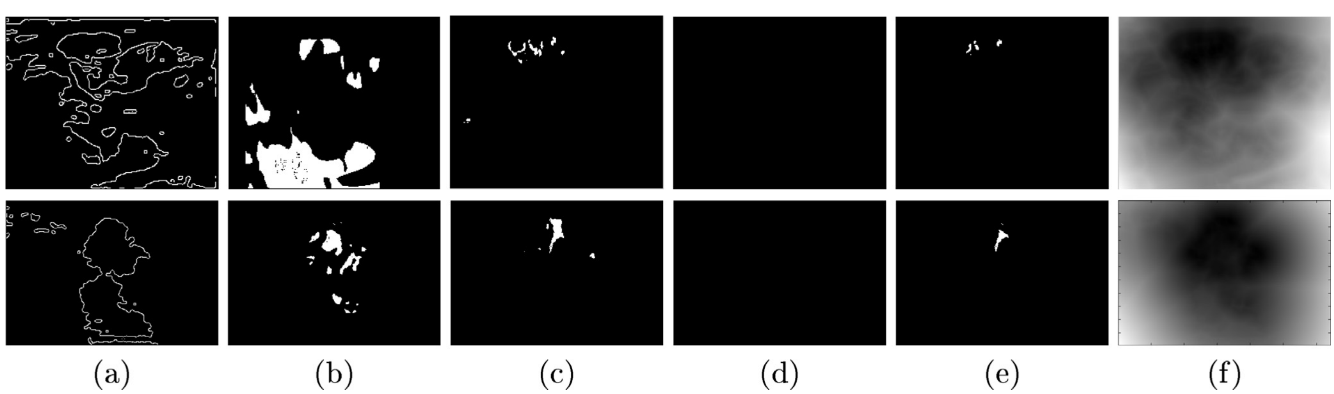

Fig. 8. Soft (top) and hard (bottom) (binary) intersection: (a) U_{edge}, (b) E, (c) D, (d) hard intersection of U_{edge}, E, and D, (e) hard intersection of E, and D, (f) soft intersection d_F.

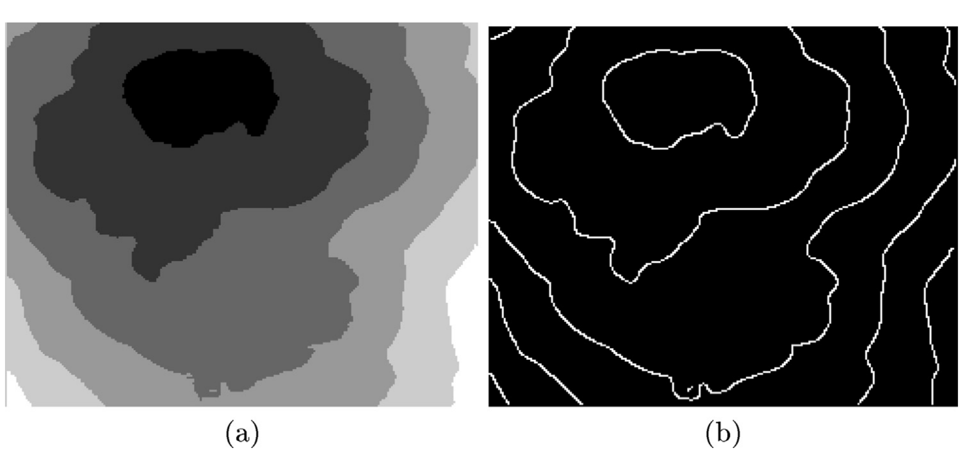

Fig. 9. (a) Quantized d_F-image (b) the corresponding contours.

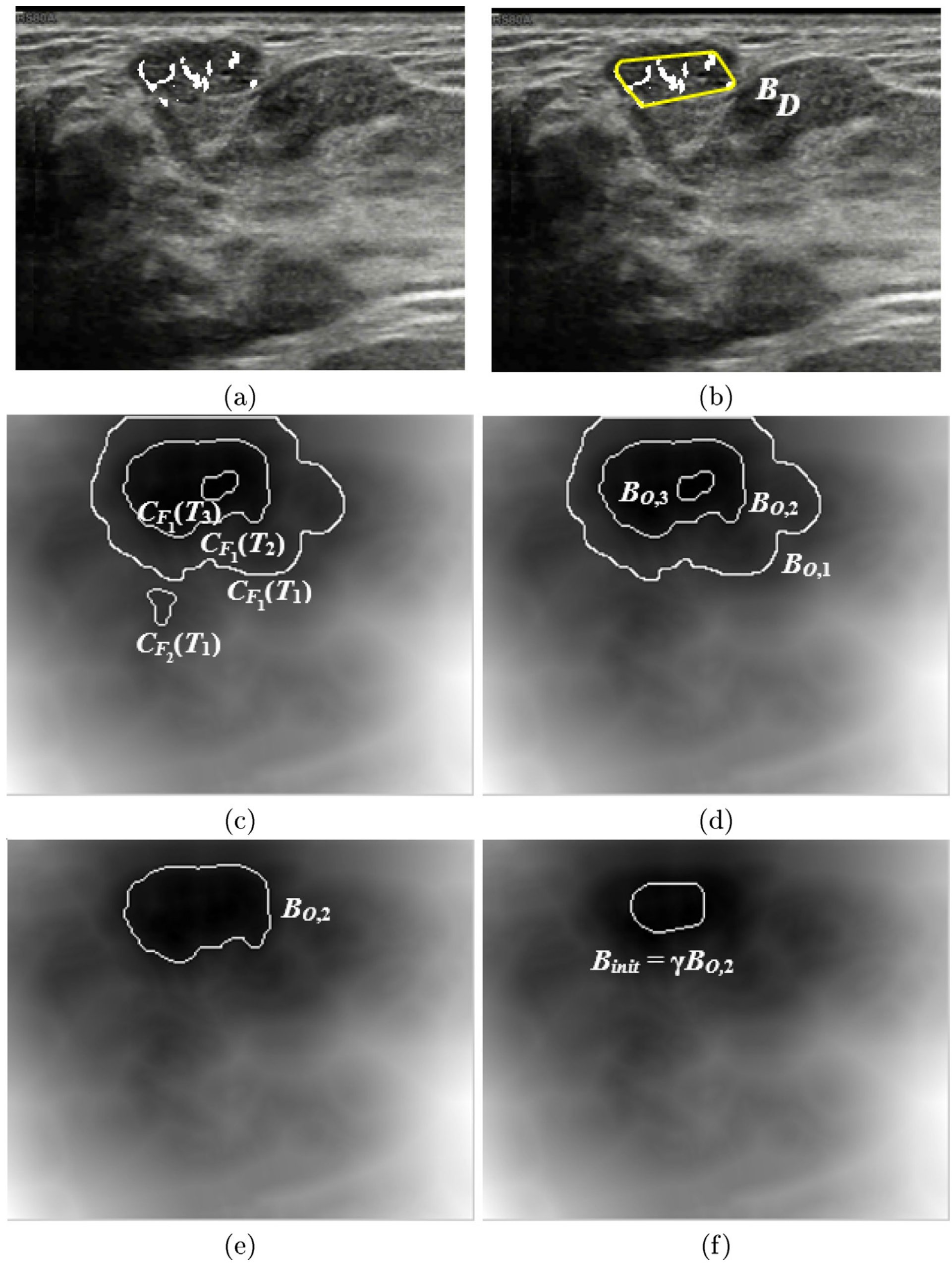

Fig. 10. (a) D-image (b) convex hull B_D overlaid with U_{raw} (c) contours $C_{F_1}(T_1), C_{F_2}(T_1)$ are obtained for $T = T_1, C_{F_1}(T_2)$, and $C_{F_1}(T_3)$ obtained for $T = T_2$, and $T = T_3$ (d) B_{o_1}, B_{o_2} and B_{o_3} are the closest to B_D (e) $B_{o,2}$ passes the decision tree (f) $B_{init} = \gamma B_{o,2}$.

where $\| \|$ denotes the Euclidean distance, X the ground truth contour, and Y the snake contour.

The averaged Hausdorff distance is defined by

$$dist_{H_2}(X,Y) = \max\left\{\frac{\sum_{a\in X}\min_{b\in Y}\|a-b\|}{L_X}, \frac{\sum_{b\in Y}\min_{a\in X}\|a-b\|}{L_Y}\right\}, \tag{14}$$

where L_X, L_Y is the length of the true contour, and the resulting contour, respectively.

The relative Hausdorff distance is given by

$$dist_{H_3}(X,Y) = \frac{dist_{H_1}(X,Y)}{L_X}\xi, \tag{15}$$

where $\xi = 1000$ is the normalizing coefficient. The distance evaluates the relative importance of the difference between the two curves. For instance, if $dist_{H_1}(X,Y) = 10$, and $L_X = 100$ pixels, the error is unacceptable, however, if for instance, $L_X = 10{,}000$, then $dist_{H_3}(X,Y)$ is appropriate. The importance of the Hausdorff distance in comparing planar curves is parametrization invariance. Although $dist_{H_1}$ is not a distance in a rigorous mathematical sense (it does not satisfy the triangle inequality), Dubuisson and Jain [20] shows that it is the best for matching curved objects.

The contour-based true positive rate is:

$$TP_c = \frac{TP_Y}{N_Y}, \tag{16}$$

where TP_Y is the number of true positive pixels, and N_Y is the total number of pixels belonging to the resulting active contour (in practice we consider $L_X = N_X$ and $L_Y = N_Y$).

5.2. Region based accuracy measures

The most used metric in validating medical segmentations [75] is the Dice coefficient given by

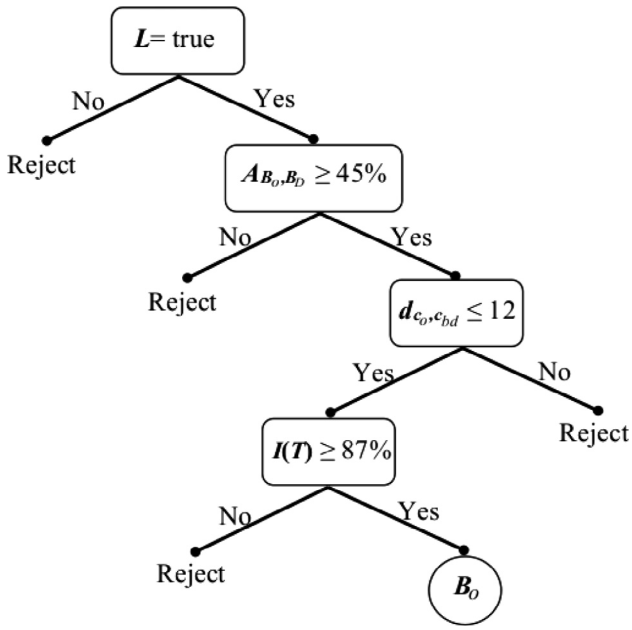

Fig. 11. Decision tree created by CART.

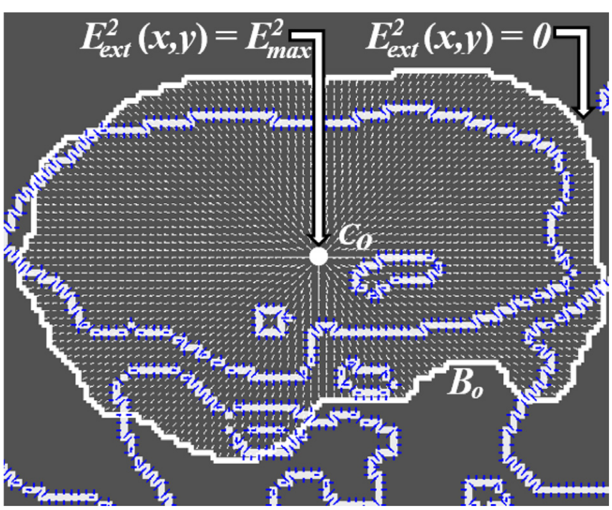

Fig. 12. Fusion snake: the conventional gradient force E^1_{ext}-blue, the proposed fusion radial force E^2_{ext}-white. (For interpretation of the references to color in this figure legend, the reader is referred to the web version of this article.)

$$DICE = \frac{2TP}{2TP + FP + FN}, \tag{17}$$

where TP, FP, and FN are the region-based true positive, false positive, and false negative. We also use the Jaccard index given by

$$JAC = \frac{TP}{TP + FP + FN}, \tag{18}$$

and the sensitivity given by

$$SEN = \frac{TP}{TP + FN}. \tag{19}$$

Finally, we employ a region based averaged Hausdorff distance, given by

$$dist_{H_R}(R_X, R_Y) = \max\left\{\frac{\sum_{a\in R_X}\min_{b\in R_Y}\|a-b\|}{A_{R_X}}, \frac{\sum_{b\in R_Y}\min_{a\in R_X}\|a-b\|}{A_{R_Y}}\right\}, \tag{20}$$

where R_X and R_Y are the regions corresponding to the contours X and Y, respectively. A_{R_X} and A_{R_Y} are the areas of R_X and R_Y, respectively.

5.3. Performance of the initialization procedure

The performance of the initialization is evaluated for the entire series of images by N_{corr}, defined as the percentage of images for which the internal and external seeds were correctly differentiated, S_{corr}, the percentage of images for which the contour was correctly segmented (the final snake is considered correct if $dist_{H_2}(X, Y) \leqslant 3$), and the computational time T_{comp}.

As noted above, the segmentation accuracy depends, not only on initialization, but on the segmentation model as well. For instance, the level set method, clustering, watershed segmentation, region growing, and edgeless active contours may benefit from the proposed FM. However, this is out of the scope of this paper. At present, the model is focused on the parametric active contours.

6. Results and discussion

6.1. Experimental dataset

The algorithm has been tested on 90 US images of breast cancer from 90 different patients obtained by a Philips iU22 ultrasound machine at the Thammasat University Hospital. The resolution ranges from 200 × 200 to 300 × 400 pixels. The ground truth contours have been drawn by three leading experts with the Department of Radiology of Thammasat University using an electronic pen and Samsung Galaxy Tablet computer. The final ground truth was obtained by the majority voting rule (two out of three).

6.2. Numerical experiments and discussion

The FM has been tested against four state-of-the-art initialization models, namely, center of divergence (CoD) [88], force field segmentation (FFS) [50], Poisson inverse gradient (PIG) [49], and quasi automatic initialization (QAI) [77,78], using the performance measures Eqs. (13)–(20). In order to prove the efficiency of the FRF, we compare it with the Vector Field Convolution (VFC) snake [48] and the recent Adaptive Diffusion Flow (ADF) [87] methods, which have been proven to be superior to GVF [90], Normal Gradient Vector Flow [40], Infinity Laplacian GVF [27], and Harmonic Gradient Vector Flow [82]. Fig. 13 is an example, comparing the initialization and the resulting snake produced by the FM/FRF with CoD/VFC, FFS/VFC,PIG/VFC, and QAI/VFC. Fig. 13(a) and (b) shows a US image with a "false" tumor on the right side of the image and a shadow at the lower left corner, characterized by grayscale comparable with the gray level of a true tumor. The resulting edge map in Fig. 13(c) shows multiple irregular contours. Clearly, if a contracting snake is initialized at the boundary of the image, it will attach itself to a wrong object and produce a totally inappropriate contour. Therefore, this US image requires a high quality initial snake, preferably expanding from the inside of the true contour. The CoD and FFS produce multiple seeds at the CoDs (Fig. 13(e) and (f)). However, due to noise, the corresponding multiple snakes are unable to merge (Fig. 13(j) and (k)). In turn, the PIG misses the true tumor and generates the initial contour inside a false object (Fig. 13 (g)). Therefore, the resulting snake is inappropriate (Fig. 13(l)). Finally, QAI requires one user-defined point inside the actual object. Due to this, QAI generates the initial contour around a correct location of the tumor. Since QAI is based on a "skeleton" of the object, which connects the CoDs, the method wrongly includes a CoD located outside the object (Fig. 13(h)). Consequently, the expanding snake grows outside the tumor and partially attaches

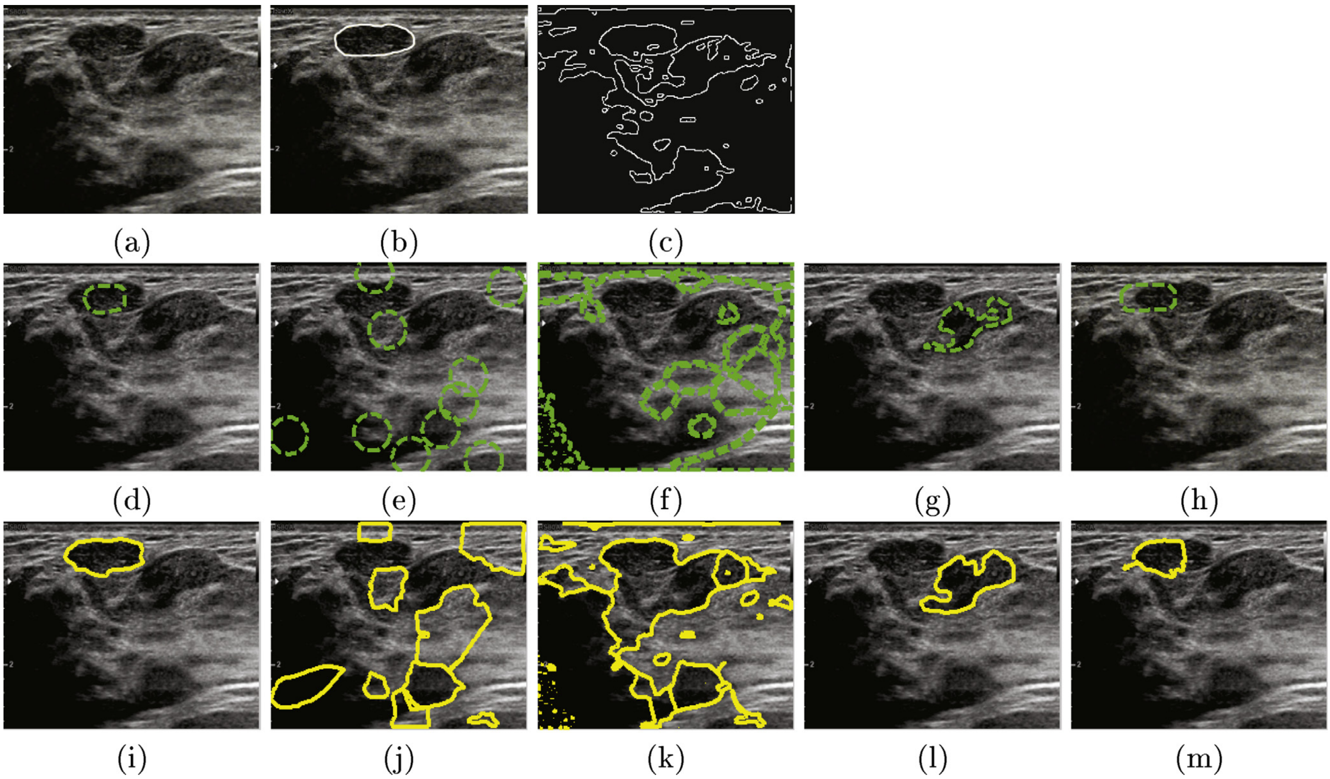

Fig. 13. (a) US image, (b) ground truth, (c) U_{edge}, (d) FM-initialization, (e) CoD initialization, (f) FFS-initialization, (g) PIG-initialization (h) QAI-initialization. Segmentation results: (i) FM/FRF (j), CoD/VFC, (k) FFS/VFC, (l)-PIG/VFC, (m) QAI/VFC.

to a false boundary (Fig. 13(m)). The FM initialization method outperforms the above techniques because it has more information about the location of the tumor. Although the low intensity mask in Fig. 2(b) cannot localize the tumor, the combination of the Doppler and elasticity images excludes the artifact (false tumor), unwanted shadows, and produces an appropriate initial contour B_{init}. Finally, the proposed DT verifies the candidate contour using supplementary features.

Tables 1–3 illustrate numerical tests of the proposed method vs. the above mentioned techniques, using the initialization and accuracy measures (13)–(20) introduced in Section 5. For every measure, we calculate the mean μ and the standard deviation σ. For all evaluation measures related to FM $\sigma/\mu < 1$. It indicates a low spread of the error.

Table 1 demonstrates the advantages of the proposed initialization method ($N_{corr} = 92.2, S_{corr} = 84.4$). The CoD and FFS failed

Table 1
Efficiency of initialization. FM vs. reference methods.

Model	Initialization measures				
	Comp. time T_{com}, sec			Correctly nitialized N_{corr}, %	Correctly segmented S_{corr}, %
	μ	σ	σ/μ		
FM	11.39	2.07	0.18	92.22	84.44
CoD	17.72	14.07	0.79	0.00	0.00
FFS	19.53	9.65	0.49	0.00	0.00
PIG	9.17	1.58	0.17	26.67	16.67
QAI	145.23	14.89	0.10	42.22	22.44

Table 2
FM vs. reference methods. Contour based measures.

Model	Contour based measures											
	H_1			H_2			H_3			TP_C		
	μ	σ	σ/μ	μ	σ	σ/μ	μ	σ	σ/μ	μ	σ	σ/μ
FM	7.54	3.40	0.45	2.40	0.95	0.39	8.27	3.43	0.41	80.73	9.32	0.11
COD	176.31	27.98	0.16	321.60	121.00	0.38	299.16	108.72	0.36	9.30	6.30	0.68
FFS	171.80	31.51	0.18	294.17	182.47	0.62	239.57	81.24	0.34	6.69	4.70	0.70
PIG	77.48	39.01	0.50	58.50	39.52	0.67	127.76	89.84	0.70	16.58	12.54	0.76
QAI	71.40	31.18	0.44	82.23	132.10	1.61	142.99	187.69	1.31	25.66	34.56	1.35

Table 3
FM vs. reference methods. Region based measures.

Model	Region based measures											
	Jaccard			*Dice*			*SEN*			H_R		
	μ	σ	σ/μ	μ	σ	σ/μ	μ	σ	σ/μ	μ	σ	σ/μ
FM	0.89	0.07	0.78	0.90	0.08	0.88	89.99	4.20	0.05	0.24	0.14	0.58
COD	0.17	0.09	0.59	0.28	0.14	0.50	31.76	21.58	0.68	74.16	28.94	0.39
FFS	0.16	0.12	0.75	0.27	0.17	0.63	36.68	29.03	0.79	62.57	34.51	0.55
PIG	0.1	0.24	2.40	0.15	0.29	1.93	12.28	24.72	2.01	42.35	11.50	0.27
QAI	0.34	0.36	1.06	0.38	0.41	1.08	38.27	34.56	0.90	44.41	38.32	0.86

($N_{corr} = S_{corr} = 0$), whereas PIG and QAI yield a lower performance ($N_{corr} = 26.7, 42.2, S_{corr} = 16.7, 22.4$, respectively). All tested methods have been implemented on the MatLab platform, using a AMD PRO A8-8600B R6 CPU, 1.6 GHz, with 8 GB RAM and 64-bit OS. The FM is the second best by the average speed (11.4 s), but significantly better in all other categories, including correctly initialized and correctly segmented images. Tables 2 and 3 show the performance of FM/FRF, CoD/VFC, FFS/VFC, PIG/VFC, and QAI/VFC. The results produced by the reference methods are characterized by low accuracy. For instance, in terms of $dist_{H_2}$, the average accuracy of the FM is 2.4 pixels, whereas for CoD, FFS, PIG, and QAI it is 321.6, 486.57, 58.5, and 82.23, respectively.

6.3. Impact of the radial force

The next important question is the impact of the FRF. Fig. 14 compares segmentation produced by the proposed FRF with that produced by VFC and ADF. Note that the initial contour is obtained by FM. Tables 4–6 clearly demonstrate that the FM-based initialization improves ADF and VFC. For instance, FM/VFC segments

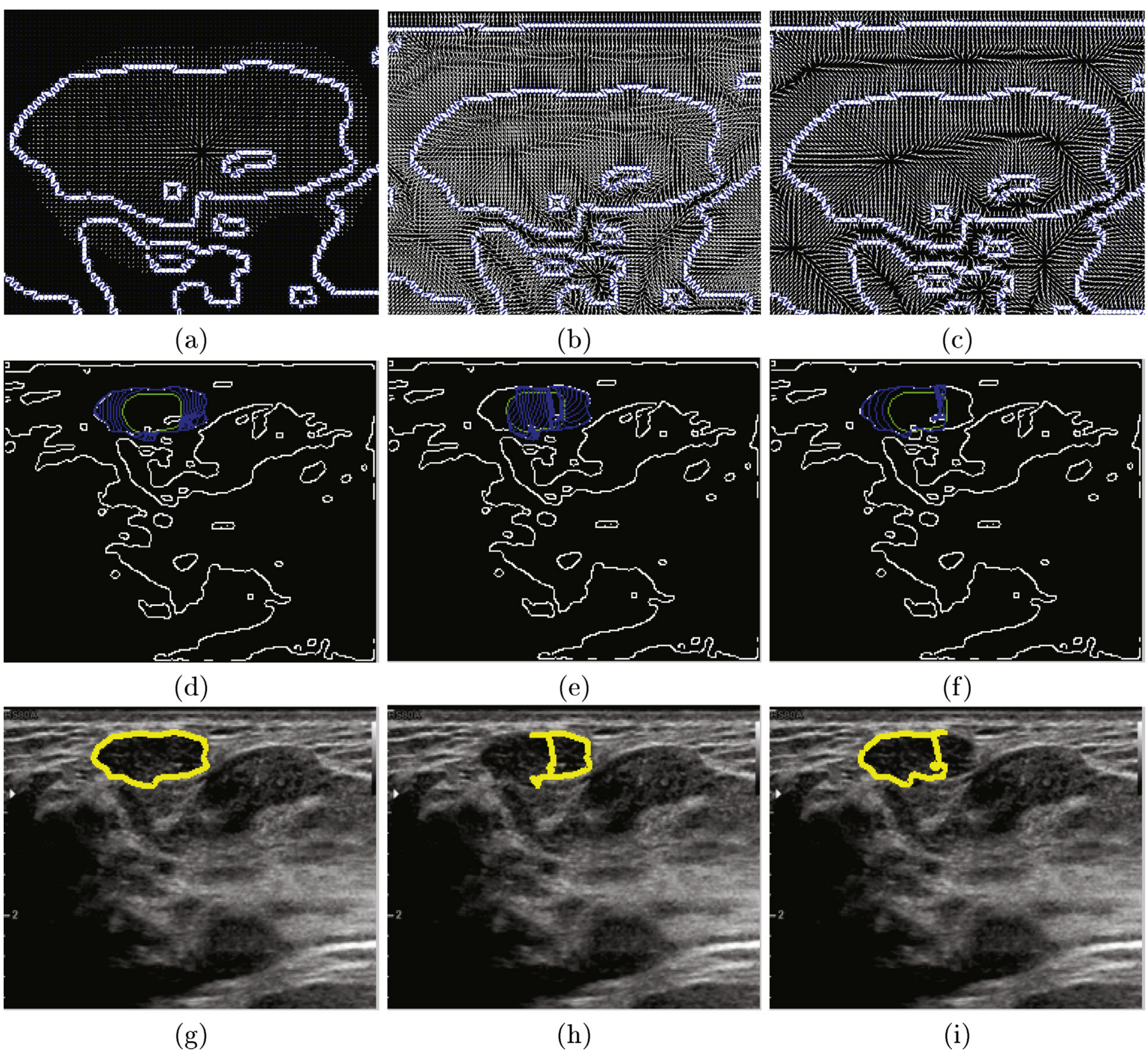

Fig. 14. Force field: (a) FRF, (b) VFC, (c) ADF; snake evolution: (d) FRF, (e) VFC, (f) ADF; segmentation results: (g) FRF, (h) VFC, (i) ADF.

Table 4
Impact of the radial force.

Model	Segmentation measures			
	Comp. Time T_{com}, sec			Correctly segmented S_{corr}, %
	μ	σ	σ/μ	
FM	0.09	0.03	0.33	84.44
VFC	0.08	0.03	0.37	56.62
ADF	0.11	0.08	0.73	43.30

Table 5
Impact of the radial force. Contour based measures.

Model	Contour based measures											
	H_1			H_2			H_3			TP_C		
	μ	σ	σ/μ	μ	σ	σ/μ	μ	σ	σ/μ	μ	σ	σ/μ
FM	7.54	3.40	0.45	2.40	0.95	0.39	8.27	3.43	0.41	80.73	9.32	0.11
VFC	20.09	18.53	0.92	6.98	9.58	1.37	13.61	10.89	0.80	62.05	28.51	0.46
ADF	24.69	20.06	0.81	7.20	9.65	1.34	14.16	10.40	0.73	61.26	25.61	0.42

Table 6
Impact of the radial force. Region based measures.

Model	Region based measures											
	Jaccard			*Dice*			*SEN*			H_R		
	μ	σ	σ/μ	μ	σ	σ/μ	μ	σ	σ/μ	μ	σ	σ/μ
FM	0.89	0.07	0.78	0.90	0.08	0.88	89.99	4.20	0.05	0.24	0.14	0.58
VFC	55.87	28.92	0.52	66.02	29.17	0.44	65.71	23.71	0.36	4.80	4.97	1.03
ADF	53.54	22.75	0.42	66.82	22.51	0.34	62.92	20.09	0.32	5.04	4.46	0.88

56% of the images, whereas the best initialization using QAI/VFC detects only about 22%. However, the performance is still substantially lower than the 84% produced by FM/FRF. The accuracy of VFC has been improved (see a decrease of H_2 from 39 pixels (PIG/VFC) to 9.58 (FM/VFC) in Table 5). However, the proposed FM/FRF shows $H_2 = 2.4$ and the smallest standard deviation of about 0.95. As a matter of fact, for the contour based measures, FM has the smallest ratio of σ/μ in all categories.

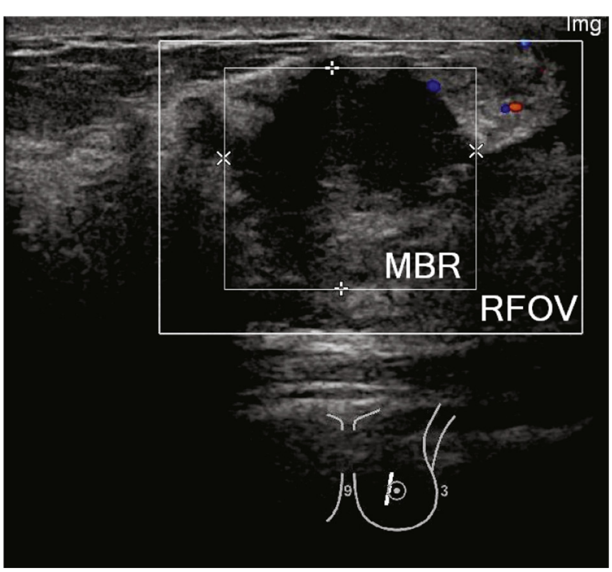

Fig. 15. Minimum bounding rectangle and the RFOV.

6.4. Reduced field of view

In clinical practice, the radiologist often defines a reduced field of view (RFOV), which can be used by a computerized segmentation procedure (see Fig. 15). Since a part of our image set does not have an RFOV, we analyzed 30 images with an RFOV defined by a radiologist. The ratio of the area of the tumor's minimum bounding rectangle (MBR) and the RFOV was approximately 1/2. Therefore for the remaining images we generated an RFOV automatically by increasing the sides of the MBR by $\sqrt{2}$. Fig. 16 displays the results obtained by FM/FRF, CoD/VFC, FFS/VFC, PIG/VFC, and QAI/VFC for a sample RFOV-image. Furthermore, Tables 7–9 compare the numerical results obtained with the RFOV. Clearly, the RFOV improved the performance of PIG and QAI to 48 and 44% respectively. However, FM also improved to 89%. Let us also compare the improvement in the accuracy taking H_2 as the reference: FM from 2.4 to 2.29, PIG from 58 to 7.7, and QAI from 82 to 8.4. Hence, RFOV has a great impact on the two reference methods, improving their accuracy by 8–10 times. However, FM still remains the best method in all categories.

6.5. Relative impact of different modalities

An important question is whether the FM/FRF requires all three image modalities, and which modality is the most important. Tables 10–12 show the accuracy of the proposed method applied to combinations (U, E), (U, D), etc. Clearly, combining the three types of images produces the best accuracy. Interestingly enough, (E, D) is the second best in accuracy ($S_{corr} = 73.3\%$). However, the segmentation procedure uses a mask produced by the US image. Since this combination implicitly uses the U-image, it is incorrect to say that the algorithm is based solely on (E, D). This complies

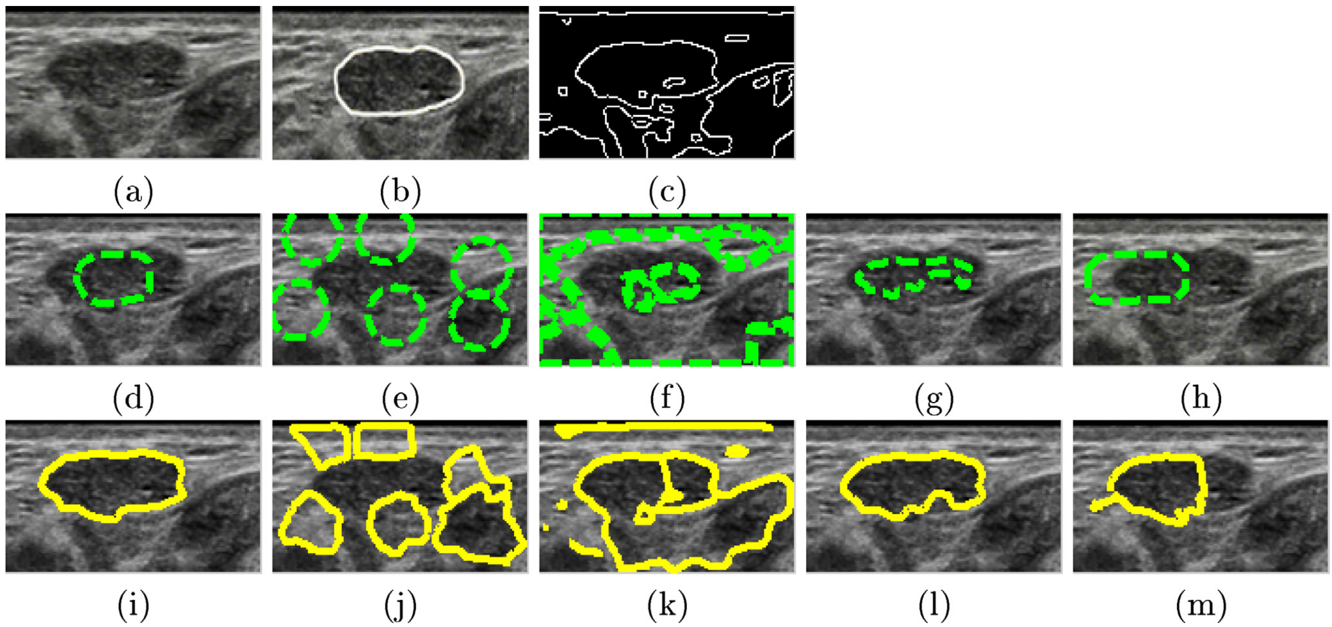

Fig. 16. Segmentation on the RFOV, (a) US image, (b) ground truth (c), U_{edge}, (d) FM-initialization, (e) CoD initialization, (f) FFS-initialization, (g) PIG-initialization (h) QAI-initialization. Segmentation results: (i) FM/FRF (j), CoD/VFC, (k) FFS/VFC, (l)-PIG/VFC, (m) QAI/VFC.

Table 7
Initialization for RFOV images.

Model	Initialization measures				
	Comp. Time T_{com}, sec			Correctly initialized N_{corr}, %	Correctly segmented S_{corr}, %
	μ	σ	σ/μ		
FM	6.58	1.75	0.26	96.67	88.89
CoD	1.54	1.37	0.89	0.00	0.00
FFS	1.62	1.65	1.02	0.00	0.00
PIG	1.47	1.17	0.79	65.56	48.89
QAI	35.32	4.79	0.13	67.76	44.45

Table 8
RFOV, contour based measures.

Model	Contour based measures											
	H_1			H_2			H_3			TP_C		
	μ	σ	σ/μ	μ	σ	μ/σ	μ	σ	μ/σ	μ	σ	σ/μ
FM	7.13	2.17	0.30	2.29	0.85	0.37	7.65	3.02	0.39	82.40	5.01	0.06
COD	43.49	8.85	0.20	33.81	16.95	0.50	61.93	18.25	0.29	32.50	18.90	0.58
FFS	42.97	9.54	0.22	34.81	15.42	0.44	54.08	17.83	0.33	26.41	6.97	0.26
PIG	25.37	21.67	0.85	7.7	9.55	1.24	16.87	13.05	0.77	68.25	26.24	0.38
QAI	26.44	21.07	0.80	8.43	9.32	1.10	18.06	12.90	0.71	65.97	24.08	0.36

Table 9
RFOV, region based measures.

Model	Region based measures											
	Jaccard			*Dice*			*SEN*			H_R		
	μ	σ	σ/μ	μ	σ	σ/μ	μ	σ	σ/μ	μ	σ	σ/μ
FM	0.90	0.05	0.55	0.91	0.06	0.66	90.53	2.56	0.03	0.18	0.07	0.39
COD	0.18	0.04	0.22	0.31	0.10	0.32	53.04	6.91	0.13	29.20	4.69	0.16
FFS	0.19	0.06	0.31	0.33	0.11	0.33	56.27	12.99	0.23	21.05	9.17	0.43
PIG	0.63	0.24	0.38	0.70	0.24	0.34	63.40	28.18	0.44	4.53	5.93	1.30
QAI	0.58	0.25	0.43	0.66	0.24	0.36	58.63	28.86	0.49	5.48	5.86	1.06

Table 10
Efficiency of initialization for different combinations of the modalities.

Model	Initialization measures				
	Comp. Time T_{com}, sec			Correctly initialized N_{corr}, %	Correctly segmented S_{corr}, %
	μ	σ	σ/μ		
FM(U, E, D)	11.39	2.07	0.18	92.00	84.44
FM(E, D)	11.29	1.78	0.16	80.00	73.33
FM(U, E)	11.26	1.91	0.17	13.33	11.11
FM(U, D)	11.30	1.79	0.16	53.33	48.88

Table 11
Contour based accuracy for different combinations of the modalities.

Model	Contour based measures											
	H_1			H_2			H_3			TP_C		
	μ	σ	σ/μ	μ	σ	σ/μ	μ	σ	σ/μ	μ	σ	σ/μ
FM(U, E, D)	7.54	3.40	0.45	2.40	0.95	0.39	8.27	3.43	0.41	80.73	9.32	0.11
FM(E, D)	12.72	9.49	0.75	3.78	3.27	0.86	13.89	12.74	0.92	77.62	22.01	0.28
FM(U, E)	42.95	41.50	0.97	30.61	40.93	1.34	138.81	102.03	0.73	9.60	26.54	2.76
FM(U, D)	17.89	10.00	0.56	5.58	3.69	0.66	19.99	14.78	0.74	56.56	31.65	0.56

Table 12
Region based accuracy for different combinations of the modalities.

Model	Region based measures											
	Jaccard			*Dice*			*SEN*			H_R		
	μ	σ	σ/μ	μ	σ	σ/μ	μ	σ	σ/μ	μ	σ	σ/μ
FM(U, E, D)	0.89	0.07	0.78	0.90	0.08	0.88	89.99	4.20	0.05	0.24	0.14	0.58
FM(E, D)	0.81	0.08	0.10	0.88	0.08	0.09	89.60	4.20	0.05	4.01	7.70	1.92
FM(U, E)	0.36	0.29	0.80	0.47	0.31	0.66	77.42	41.15	0.53	37.10	21.53	0.58
FM(U, D)	0.60	0.21	0.35	0.73	0.21	0.29	84.21	14.79	0.17	7.40	7.67	1.04

with recent clinical research [18,25], which reports that the Doppler image alone does not significantly contribute to categorization of solid masses.

6.6. Limitations of the method

The method requires a good quality Doppler image D_{raw}. If D_{raw} does not present a well-defined cluster of Doppler spots, the procedure works in the $U-E$ mode, which may reduce the accuracy of segmentation (see Table 10). Some low grade cancers may not appear in the Doppler images. For instance, Adler et al. [2] reports that "four percent of the cancers had no detectable [Doppler] flow".

7. Conclusions

The proposed new automatic procedure for initialization of active contours, applied to the segmentation of ultrasound images of breast cancer, outperforms preceding algorithms. The procedure includes FM initialization and a radial force based on the fusion of the conventional US, Doppler, and elasticity images. Although it requires training a decision tree, the procedure is also automatic. We conjecture that the proposed algorithm is applicable to similar US images without any modifications.

Acknowledgement

We wish to thank the Associate Editor of the journal Dr. Spyretta Golemati and anonymous reviewers for their insightful comments. This research is sponsored by the Thailand Research Fund, grant BRG5780012, and the Center of Excellence in Biomedical Engineering, Thammasat University.

References

[1] Breast Cancer Facts and Figures, Oct 2017. <https://www.cancer.org/research/cancer-facts-statistics/breast-cancer-facts-figures.html>.
[2] D. Adler, P. Carson, J. Rubin, D. Quinn-Reid, C. Kanan, G. Cottrell, Doppler ultrasound color flow imaging in the study of breast cancer: preliminary findings, Ultrasound Med. Biol. 16 (6) (1990) 553–559.
[3] Y.S. Akgul, C. Kambhamettu, M. Stone, Extraction and tracking of the tongue surface from ultrasound image sequences, in: Proceedings. IEEE Computer Society Conference on Computer Vision and Pattern Recognition, Jun 1998, pp. 298–303.
[4] A. Athanasiou, A. Tardivon, M. Tanter, B. Sigal-Zafrani, J. Bercoff, T. Deffieux, J.L. Gennisson, M. Fink, S. Neuenschwander, Breast lesions: quantitative elastography with supersonic shear imaging-preliminary results, Radiology 256 (2010) 297–303.
[5] W.A. Berg, D.O. Cosgrove, C.J. Doré, F.K.W. Schäfer, W.E. Svensson, R.J. Hooley, R. Ohlinger, E.B. Mendelson, C. Balu-Maestro, M. Locatelli, C. Tourasse, B.C. Cavanaugh, V. Juhan, A.T. Stavros, A. Tardivon, J. Gay, J.P. Henry, C. Cohen-Bacrie, Shear-wave elastography improves the specificity of breast US: the BE1 multinational study of 939 masses, Radiology 262 (2012) 435–449.
[6] J.C. Bezdek, Pattern Recognition with Fuzzy Objective Function Algorithms, Kluwer Academic Publishers, Norwell, MA, USA, 1981.
[7] K.S.S. Bhatia, A.C.L. Lam, S.W.A. Pang, D. Wang, A.T. Ahuja, Feasibility study of texture analysis using ultrasound shear wave elastography to predict malignancy in thyroid nodules, Ultrasound Med. Biol. 42 (7) (2016) 1671–1680.
[8] D. Boukerroui, A. Baskurt, J.A. Noble, O. Basset, Segmentation of ultrasound images – multiresolution 2D and 3D algorithm based on global and local statistics, Pattern Recogn. Lett. 24 (2003) 779–790.
[9] L. Breiman, J. Friedman, R. Olshen, C. Stone, Classification and Regression Trees, Wadsworth and Brooks, Monterey, CA, 1984.
[10] R.G. Brereton, The chi squared and multinormal distributions, J. Chemom. 29 (1) (2015) 9–12.
[11] R.G. Brereton, The Mahalanobis distance and its relationship to principal component scores, J. Chemom. 29 (3) (2015) 143–145.

[12] Y.C. Chang, Y.H. Huang, C.S. Huang, R.F. Chang, Vascular morphology and tortuosity analysis of breast tumor inside and outside contour by 3D power Doppler ultrasound, Ultrasound Med. Biol. 38 (11) (2012) 1859–1869.

[13] H.D. Cheng, J. Shan, W. Ju, Y. Guo, L. Zhang, Automated breast cancer detection and classification using ultrasound images: a survey, Pattern Recogn. 43 (2010) 299–317.

[14] J. Cheng, S.W. Foo, Dynamic directional gradient vector flow for snakes, IEEE Trans. Image Process. 15 (6) (2006) 1563–1571.

[15] N. Cho, M. Jang, C.Y. Lyou, J.S. Park, H.Y. Choi, W.K. Moon, Distinguishing benign from malignant masses at breast US: combined US elastography and color Doppler US – influence on radiologist accuracy, Radiology 262 (1) (2012) 80–90.

[16] I. Cohen, I. Herlin, A motion computation and interpretation framework for oceanographic satellite images, in: Proceedings of International Symposium on Computer Vision – ISCV, Nov 1995, pp. 13–18.

[17] D. Coppersmith, S.J. Hong, J.R. Hosking, Partitioning nominal attributes in decision trees, Data Min. Knowl. Discov. 3 (2) (1999) 197–217.

[18] Y. Davoudi, B. Borhani, M.P. Rad, N. Matin, The role of Doppler sonography in distinguishing malignant from benign breast lesions, J. Med. Ultrasound 22 (2) (2014) 92–95.

[19] D.J. Doshi, D.E. March, G.M. Crisi, B.F. Coughlin, Complex cystic breast masses: diagnostic approach and imaging-pathologic correlation, RadioGraphics 27 (suppl_1) (2007) S53–S64.

[20] M.P. Dubuisson, A.K. Jain, A modified Hausdorff distance for object matching, in: Proceedings of 12th International Conference on Pattern Recognition, vol. 1, 1994, pp. 566–568.

[21] J.R. Eisenbrey, J.K. Dave, F. Forsberg, Recent technological advancements in breast ultrasound, Ultrasonics 70 (2016) 183–190.

[22] A. Elkharbotly, H.M. Farouk, Ultrasound elastography improves differentiation between benign and malignant breast lumps using b-mode ultrasound and color Doppler, Egypt. J. Radiol. Nucl. Med. 46 (4) (2015) 1231–1239.

[23] Y. Feng, F. Dong, X. Xia, C.H. Hu, Q. Fan, Y. Hu, M. Gao, S. Mutic, An adaptive fuzzy c-means method utilizing neighboring information for breast tumor segmentation in ultrasound images, Med. Phys. 44 (2017) 3752–3760.

[24] K. Fergani, D. Lui, C. Scharfenberger, A. Wong, D. Clausi, Hybrid structural and texture distinctiveness vector field convolution for region segmentation, Comput. Vis. Image Underst. 125 (2014) 85–96.

[25] G. Gokalp, U. Topal, E. Kizilkaya, Power Doppler sonography: anything to add to BI-RADS US in solid breast masses?, Eur J. Radiol. 70 (1) (2009) 77–85.

[26] P. Gu, W.M. Lee, M. Roubidoux, J. Yuan, X. Wang, P.L. Carson, Automated 3D ultrasound image segmentation to aid breast cancer image interpretation, Ultrasonics 65 (2016) 51–58.

[27] L. Guillot, C. Le Guyader, Extrapolation of Vector Fields Using the Infinity Laplacian and with Applications to Image Segmentation, Springer, Berlin, Heidelberg, 2009, pp. 87–99.

[28] Y. Guo, A. Sengur, J.W. Tian, A novel breast ultrasound image segmentation algorithm based on neutrosophic similarity score and level set, Comput. Methods Programs Biomed. 123 (2016) 43–53.

[29] D. Gupta, R. Anand, A hybrid edge-based segmentation approach for ultrasound medical images, Biomed. Signal Process. Control 123 (2016) 43–53.

[30] L. He, Z. Peng, B. Everding, X. Wang, C. Han, K. Weiss, W. Wee, A comparative study of deformable contour methods on medical image segmentation, Image Vis. Comput. 26 (2008) 141–163.

[31] Y.H. Hsiao, Y.L. Huang, S.J. Kuo, W.M. Liang, S.T. Chen, D.R. Chen, Characterization of benign and malignant solid breast masses in harmonic 3D power Doppler imaging, Eur. J. Radiol. 71 (1) (2009) 89–95.

[32] C.Y. Hsu, C.Y. Liu, C.M. Chen, Automatic segmentation of liver {PET} images, Comput. Med. Imaging Graph. 32 (7) (2008) 601–610.

[33] C.Y. Hsu, H.F. Wang, H.C. Wang, K.K. Tseng, Automatic extraction of face contours in images and videos, Future Gener. Comput. Syst. 28 (1) (2012) 322–335.

[34] Q.H. Huang, S.Y. Lee, L.-Z. Liu, M.H. Lu, L.W. Jin, A.H. Li, A robust graph-based segmentation method for breast tumors in ultrasound images, Ultrasonics 52 (2012) 266–275.

[35] Y. Huang, D. Chen, Watershed segmentation for breast tumor in 2-D sonography, Ultrasound Med. Biol. 30 (2004) 623–625.

[36] Y.L. Huang, S.J. Kuo, C.C. Hsu, H.S. Tseng, Y.H. Hsiao, D.R. Chen, Computer-aided diagnosis for breast tumors by using vascularization of 3D power Doppler ultrasound, Ultrasound Med. Biol. 35 (10) (2009) 1607–1614.

[37] M.A. Hussain, F. Alam, S.A. Rupa, R. Awwal, S.Y. Lee, K. Hasan, Lesion edge preserved direct average strain estimation for ultrasound elasticity imaging, Ultrasonics 54 (1) (2014) 137–146.

[38] R. Ibrahim, K. Rahmat, F. Fadzli, F.I. Rozalli, C.J. Westerhout, K. Alli, A. Vijayananthan, F. Moosa, Evaluation of solid breast lesions with power Doppler: value of penetrating vessels as a predictor of malignancy, Singapore Med. J. 57 (11) (2016) 634–640.

[39] A. Itoh, E. Ueno, E. Tohno, H. Kamma, H. Takahashi, T. Shiina, M. Yamakawa, T. Matsumura, Breast disease: clinical application of US elastography for diagnosis, Radiology 239 (2006) 341–350.

[40] N. Jifeng, W. Chengke, L. Shigang, Y. Shuqin, NGVF: an improved external force field for active contour model, Pattern Recogn. Lett. 28 (1) (2007) 58–63.

[41] I.S. Jung, D. Thapa, G.N. Wang, Automatic Segmentation and Diagnosis of Breast Lesions Using Morphology Method Based on Ultrasound, Springer, Berlin, Heidelberg, 2005, pp. 1079–88.

[42] C. Kanan, G. Cottrell, Color-to-grayscale: does the method matter in image recognition?, PLoS ONE 7 (1) (2012) 1–7

[43] M. Kass, A. Witkin, D. Terzopoulos, Snakes: active contour models, Int. J. Comput. Vision 1 (4) (1988) 321–331.

[44] K. Kirimasthong, A. Rodtook, U. Chaumrattanakul, S.S. Makhanov, Phase portrait analysis for automatic initialization of multiple snakes for segmentation of the ultrasound images of breast cancer, Pattern Anal. Appl. 20 (1) (2017) 239–251.

[45] T. Kolb, J. Lichy, J. Newhouse, Comparison of the performance of screening mammography, physical examination, and breast US and evaluation of factors that influence them: an analysis of 27,825 patients evaluations, Radiology 225 (2002) 165–175.

[46] R. Laganiere, OpenCV 3 Computer Vision Application Programming Cookbook, third ed., Packt Publishing, 2017.

[47] Y.C. Lai, Y.S. Huang, D.W. Wang, C.M. Tiu, Y.H. Chou, R.F. Chang, Computer-aided diagnosis for 3D power Doppler breast ultrasound, Ultrasound Med. Biol. 39 (4) (2013) 555–567.

[48] B. Li, S.T. Acton, Active contour external force using vector field convolution for image segmentation, IEEE Trans. Image Process. 16 (8) (2007) 2096–2106.

[49] B. Li, S.T. Acton, Automatic active model initialization via poisson inverse gradient, IEEE Trans. Image Process. 17 (8) (2008) 1406–1420.

[50] C. Li, J. Liu, M.D. Fox, Segmentation of external force field for automatic initialization and splitting of snakes, Pattern Recogn. 38 (11) (2005) 1947–1960.

[51] J. Li, W.Y. Yau, H. Wang, Constrained nonlinear models of fingerprint orientations with prediction, Pattern Recogn. 39 (1) (2006) 102–114.

[52] J. Li, W.Y. Yau, H. Wang, Combining singular points and orientation image information for fingerprint classification, Pattern Recogn. 41 (1) (2008) 353–366.

[53] L. Li, X. Zhou, X. Zhao, S. Hao, J. Yao, W. Zhong, H. Zhi, B-mode ultrasound combined with color Doppler and strain elastography in the diagnosis of non-mass breast lesions: a prospective study, Ultrasound Med. Biol. 43 (11) (2017) 2582–2590.

[54] B. Liu, H. Cheng, J. Huang, J. Tian, J. Liu, J. Tang, Automated segmentation of ultrasonic breast lesions using statistical texture classification and active contour based on probability distance, Ultrasound Med. Biol. 35 (2008) 1309–1324.

[55] S. Liu, Y. Peng, A local region-based Chan-Vese model for image segmentation, Pattern Recogn. 45 (7) (2012) 2769–2779.

[56] W.Y. Loh, Regression trees with unbiased variable selection and interaction detection, Stat. Sin. 12 (2) (2002) 361–386.

[57] W.Y. Loh, Y.S. Shin, Split selection methods for classification trees, Stat. Sin. 7 (4) (1997) 815–840.

[58] A. Madabhushi, D.N. Metaxas, Combining low-, high-level and empirical domain knowledge for automated segmentation of ultrasonic breast lesions, IEEE Trans. Med. Imag. 22 (2) (2003) 155–169.

[59] H. Madjar, Role of breast ultrasound for the detection and differentiation of breast lesions, Breast Care (Basel) 5 (2) (2010) 109–114.

[60] P.C. Mahalanobis, On the generalized distance in statistics, Proc. Natl. Inst. Sci. (Calcutta) 2 (1936) 49–55.

[61] MathLab: Fitctree Function, the Fit Binary Classification Decision Tree for Multiclass Classification, Oct 2017. <https://ch.mathworks.com/help/stats/fitctree.html>.

[62] W.K. Moon, I.L. Chen, J.M. Chang, S.U. Shin, C.M. Lo, R.F. Chang, The adaptive computer-aided diagnosis system based on tumor sizes for the classification of breast tumors detected at screening ultrasound, Ultrasonics 76 (2017) 70–77.

[63] W.K. Moon, Y.S. Huang, Y.W. Lee, S.C. Chang, C.M. Lo, M.C. Yang, M.S. Bae, S.H. Lee, J.M. Chang, C.S. Huang, Y.T. Lin, R.F. Chang, Computer-aided tumor diagnosis using shear wave breast elastography, Ultrasonics 78 (2017) 125–133.

[64] W.K. Moon, J.G. Im, D.Y. Noh, M.C. Han, Nonpalpable breast lesions: evaluation with power Doppler US and a microbubble contrast agent-initial experience, Radiology 217 (1) (2000) 240–246.

[65] J. Noble, D. Boukerroui, Ultrasound image segmentation: a survey, IEEE Trans. Med. Imag. 25 (2006) 987–1010.

[66] I. Petridis, M. Barbagianni, K. Ioannidi, E. Samaras, G. Fthenakis, E. Vloumidi, Doppler ultrasonographic examination in sheep, Small Ruminant Res. 152 (2017) 22–32.

[67] N. Ray, S.T. Acton, T. Altes, E.E. de Lange, J.R. Brookeman, Merging parametric active contours within homogeneous image regions for MRI-based lung segmentation, IEEE Trans. Med. Imag. 22 (2) (2003) 189–199.

[68] A. Rodtook, S. Makhanov, Multi-feature gradient vector flow snakes for adaptive segmentation of the ultrasound images of breast cancer, J. Vis. Commun. Image Represent. 24 (8) (2013) 1414–1430.

[69] N.S.E. Saghir, C.A. Adebamowo, B.O. Anderson, R.W. Carlson, P.A. Bird, M. Corbex, R.A. Badwe, M.A. Bushnaq, A. Eniu, J.R. Gralow, J.K. Harness, R. Masetti, F. Perry, M. Samiei, D.B. Thomas, B. Wiafe-Addai, E. Cazap, Breast cancer management in low resource countries (LRCs): consensus statement from the breast health global initiative, Breast 20 (Supplement 2) (2011) S3–S11.

[70] B.N. Saha, N. Ray, H. Zhang, Snake validation: a PCA-based outlier detection method, IEEE Signal Process. Lett. 16 (6) (2009) 549–552.

[71] S. Selvan, S.S. Devi, Automatic seed point selection in ultrasound echography images of breast using texture features, Biocybernetics Biomed. Eng. 35 (3) (2015) 157–168.

[72] J. Shan, H. Cheng, Y. Wang, Completely automated segmentation approach for breast ultrasound images using multiple-domain features, Ultrasound Med. Biol. 38 (2012) 262–275.

[73] M.K. Shetty, Screening and diagnosis of breast cancer in low-resource countries: what is state of the art?, Seminars Ultrasound CT MRI 32 (4) (2011) 300–305
[74] C.F. Shu, R.C. Jain, Vector field analysis for oriented patterns, IEEE Trans. Pattern Anal. Mach. Intell. 16 (9) (1994) 946–950.
[75] A. Taha, A. Hanbury, Metrics for evaluating 3D medical image segmentation: analysis, selection, and tool, BMC Med. Imag. (2015) 15–29.
[76] J. Tang, A multi-direction GVF snake for the segmentation of skin cancer images, Pattern Recogn. 42 (6) (2009) 1172–1179.
[77] C. Tauber, H. Batatia, A. Ayache, A general quasi-automatic initialization for snakes: application to ultrasound images, in: IEEE International Conference on Image Processing 2005, vol. 2, Sept 2005, pp. II-806–9.
[78] C. Tauber, H. Batatia, A. Ayache, Quasi-automatic initialization for parametric active contours, Pattern Recogn. Lett. 31 (1) (2010) 83–90.
[79] A. Thomas, M. Warm, M. Hoopmann, F. Diekmann, T. Fischer, Tissue Doppler and strain imaging for evaluating tissue elasticity of breast lesions, Acad. Radiol. 14 (5) (2007) 522–529.
[80] X. Tian, S. Sammaraighe, G. Murphy, An integrated algorithm for detecting position and size of knots on logs using texture analysis, in: Image and Visions Computing, 1999, pp. 121–132.
[81] E. Veronese, R. Stramare, A. Campion, B. Raffeiner, V. Beltrame, E. Scagliori, A. Coran, L. Ciprian, U. Fiocco, E. Grisan, Improved detection of synovial boundaries in ultrasound examination by using a cascade of active-contours, Med. Eng. Phys. 35 (2) (2013) 188–194.
[82] Y. Wang, Y. Jia, L. Liu, Harmonic gradient vector flow external force for snake model, Electron. Lett. 44 (2) (2008) 105–106.
[83] Y. Wang, J. Liang, Y. Jia, On the Critical Point of Gradient Vector Flow Snake, Springer, Berlin, Heidelberg, 2007, pp. 754–763.
[84] Z.L. Wang, L. Sun, Y. Li, N. Li, Relationship between elasticity and collagen fiber content in breast disease: a preliminary report, Ultrasonics 57 (2015) 44–49.
[85] M. Wei, Y. Zhou, M. Wan, A fast snake model based on non-linear diffusion for medical image segmentation, Comput. Med. Imag. Graph. 28 (3) (2004) 109–117.
[86] WHO: Breast Cancer: Prevention and Control, Oct 2017. <http://www.who.int/cancer/detection/breastcancer/en/>.
[87] Y. Wu, Y. Wang, Y. Jia, Adaptive diffusion flow active contours for image segmentation, Comput. Vis. Image Underst. 117 (10) (2013) 1421–1435.
[88] G. Xingfei, T. Jie, An automatic active contour model for multiple objects, in: Object Recognition Supported by User Interaction for Service Robots, vol. 2, pp. 881–884.
[89] C. Xu, J.L. Prince, Generalized gradient vector flow external forces for active contours, Signal Process. 71 (2) (1998) 131–139.
[90] C. Xu, J.L. Prince, Snakes, shapes, and gradient vector flow, IEEE Trans. Image Process. 7 (3) (1998) 359–369.
[91] M. Yagtu, E. Turan, C.O. Turan, The role of ultrasonographic elastography in the differential diagnosis of breast masses and its contribution to classical ultasonographic evaluation, J. Breast Health 10 (2014) 141–146.
[92] Y. Yamakoshi, T. Nakajima, T. Kasahara, M. Yamazaki, R. Koda, N. Sunaguchi, Shear wave imaging of in vivo breast tissue by color Doppler shear wave elastography, IEEE Trans. Ultrasonics Ferroelectr. Frequency Control 64 (2) (2017) 340–348.
[93] W.Y. Yau, J. Li, H. Wang, Nonlinear phase portrait modeling of fingerprint orientation, in: ICARCV 2004 8th Control, Automation, Robotics and Vision Conference, 2004, vol. 2, Dec 2004, pp. 1262–1267.
[94] D. Yuan, H. Chia, H. Wang, Optimal multi-level thresholding using a two-stage Otsu optimization approach, Pattern Recogn. Lett. 30 (2009) 275–284.
[95] H. Yuan, L. Yupin, H. Dongcheng, Semi-automatic initialization of gradient vector flow snakes, J. Electron. Imag. 15 (4) (2006) 043006–043008.
[96] Q. Zhang, Y. Xiao, W. Dai, J. Suo, C. Wang, J. Shi, H. Zheng, Deep learning based classification of breast tumors with shear-wave elastography, Ultrasonics 72 (2016) 150–157.